Characterization of the multiple equilibria regime in a global ocean model

By HENK A. DIJKSTRA*, *Institute for Marine and Atmospheric Research Utrecht, Department of Physics and Astronomy, Utrecht University, Princetonplein 5, 3584 Utrecht, the Netherlands*

ABSTRACT

Low-resolution global ocean models display hysteresis behaviour when forced with an anomalous freshwater input into the northern North Atlantic. Of central importance in this hysteresis behaviour is the existence of so-called saddle-node bifurcations. In this paper, focus is on the physical characterization of the multiple equilibrium regime using a fully implicit global ocean model for which bifurcation diagrams can be explicitly computed. The physics of the position of the relevant saddle-node bifurcation in parameter space is clarified and a modification of an earlier suggested diagnostic of the presence of the multiple equilibrium regime is proposed. The relevance of this indicator for coupled climate models is shown by studying the sensitivity of the multiple equilibria regime to changes in the horizontal and vertical diffusivities of the model.

1. Introduction

Major transitions in the ocean circulation have not been documented in the instrumental record (Bryden et al., 2005). There is a real possibility, however that more than one time-mean flow pattern of the global ocean circulation, and in particular of the Atlantic Meridional Overturning Circulation (AMOC), may exist under the present forcing conditions. Reconstructions of ocean deep temperatures during the last glacial period have provided ample evidence that rapid climate changes were associated with major changes in the deep current structure in the Atlantic (Clark et al., 2002). The existence of at least one additional state of the global ocean circulation, with a substantially different meridional heat transport, would have important consequences for climate variability and global climate change over the next century (McAvaney, 2001). It is therefore of central importance to determine whether the present time-mean ocean circulation state is unique or in a multiple equilibria regime.

After the early work of Stommel (1961), the interest in the multiple equilibria regime revived when Bryan (1986) showed that such a regime is in principle consistent with the governing equations of the three-dimensional ocean circulation. Since then, many studies have demonstrated that multiple equilibria exist in a hierarchy of global ocean models and ocean–atmosphere models (Stocker et al., 1992; Rahmstorf, 1995; Manabe and Stouffer, 1999). These studies can be divided into three classes: (i) those

*Correspondence
e-mail: dijkstra@phys.uu.nl

that focus on the behaviour of the time-mean circulation under (controlled) changes in the freshwater flux pattern and amplitude (also called 'hosing experiments'); (ii) those that focus on the temporal evolution of the meridional overturning circulation due to specified changes in the (initial) salinity field under otherwise fixed parameter values and forcing conditions and (iii) studies with coupled ocean–atmosphere models where the climate response due to the increase of atmospheric greenhouse gases is considered.

The sensitivity of the AMOC to anomalous freshwater input into the northern North Atlantic has been investigated by adding freshwater at a very slow rate such that quasi-steady states are monitored in time (Rahmstorf, 2000). In this way, a first impression of the stable equilibria of the global ocean circulation can be obtained. In several global ocean models it was found that the present day AMOC collapses when the freshwater input is large enough. When the freshwater forcing is reversed from the collapsed state, hysteresis behaviour occurs because the collapsed state can be maintained under substantial positive freshwater-flux anomalies. This hysteresis behaviour has been found in many low-resolution ocean models and Earth system Models of Intermediate Complexity (EMICs). The position of the unperturbed state (no anomalous freshwater input) is in the multiple equilibrium regime for some models but for others it is in the unique regime (Rahmstorf et al., 2005).

A typical example of the second class of studies is the one by Vellinga et al. (2002) that investigated the response of a coupled ocean–atmosphere model (HadCM3) to a sudden decrease in surface salinity in the northern North Atlantic. The overturning circulation first reduced substantially but it recovered after about

120 yr. The salt transport by the subtropical gyre appeared a crucial factor in the recovery process since it is able to restore the salt deficit caused by the initial perturbation.

In studies where the atmospheric CO_2 is increased, some models predict a collapse of the Atlantic meridional overturning whereas others show only a modest change (McAvaney, 2001). In the work of Manabe and Stouffer (1994, 1999), the increase of CO_2 leads to a significant weakening of the Atlantic meridional overturning circulation; at the time of CO_2 doubling, it has decreased by 80%. If the CO_2 level is then held fixed, the overturning recovers on a century timescale. However, when the CO_2 concentration is again doubled over the next 70 yr, the Atlantic meridional overturning completely collapses and does not recover. In contrast, other transient climate simulation studies with increasing CO_2 find only a relatively modest reduction (Wood et al., 1999) or no reduction at all (Latif et al., 2000) in the Atlantic overturning. The mechanisms for this behaviour have been analysed for some cases (Thorpe et al., 2001) and are related to a stabilizing salt transport by the ocean flow.

For all these type of studies there is a wide spread in the behaviour of the different models around (Schmittner et al., 2005; Stouffer et al., 2006). A prominent example illustrating the sensitivity of models to small variations in parameters are the hosing experiments by Manabe and Stouffer (1999). In the GFDL climate model they first consider the standard case of a vertically dependent mixing coefficient (with slightly larger values at depth than near the surface) of heat and salt (Bryan and Lewis, 1979), indicated here by K_V. When the equilibrium state obtained after spinup is perturbed with a large anomalous freshwater perturbation, the AMOC collapses and the collapsed state appears stable when the freshwater forcing is removed. In a second case, the value of K_V is taken constant but relatively large. When the equilibrium state obtained after spinup is perturbed with a similar freshwater perturbation, the AMOC also collapses but it recovers when the anomalous freshwater forcing is released. Although these are results of only a few simulations they illustrate that apparently a small change in a parameter, such as the vertical diffusivity, may already move the unperturbed state from the multiple equilibrium regime to the unique regime.

In this paper, we focus on the physical processes that characterize the multiple equilibrium regime in a global ocean model. In a recent paper, De Vries and Weber (2005) have provided results of an EMIC study that indicate that the freshwater budget over the North Atlantic is a key factor for the existence of the multiple equilibrium regime. This was also already mentioned in Rahmstorf (1996) but the precise relation between the Atlantic freshwater budget and the different flow regimes has not been considered in an ocean General Circulation Model (GCM), EMIC or coupled GCM. A systematic investigation can be performed by using numerical techniques, so-called continuation methods, which compute the regime boundaries explicitly. Recently, a bifurcation analysis was performed using a model of the global ocean circulation that is coupled to an energy-balance

model of the atmosphere (Weijer et al., 2003; Dijkstra and Weijer, 2005). With continuation techniques, one can efficiently calculate the steady states of this model versus model parameters (Dijkstra, 2005).

Although this fully implicit ocean model has to be improved in several aspects, the present model and the numerical techniques are in a stage that a more systematic determination of the sensitivity of the different regimes (unique versus multiple equilibrium) to parameter variations can be made. In this paper, bifurcation diagrams for different horizontal and vertical diffusivities are presented. Using the Atlantic freshwater budget, the position of the saddle-node bifurcations bounding the multiple equilibrium regime in parameter space is characterized. This characterization is subsequently used to study the physics of the sensitivity of the multiple equilibrium regime to changes in the horizontal and vertical diffusivities.

2. Formulation

In this section, we will shortly recall the model used (Section 2.1) and summarize the continuation approach (Section 2.2) which is applied to this model to compute the bifurcation diagrams.

2.1. Model

The description of the fully implicit global ocean model used in this study is presented in Weijer et al. (2003) and Dijkstra and Weijer (2005) to which the reader is referred for full details. The governing equations of the ocean model are the hydrostatic, primitive equations in spherical coordinates on a global domain which includes full continental geometry as well as bottom topography. The ocean velocities in eastward and northward directions are indicated by u and v, the vertical velocity is indicated by w, the pressure by p and the temperature and salinity by T and S, respectively. The horizontal resolution of the model is about $4°$ (a 96×38 Arakawa C-grid on a domain [180° W, 180° E] × [85.5°S, 85.5°N]) and the grid has 12 levels in the vertical. The vertical grid is non-equidistant with the most upper (lowest) layer having a thickness of 50 m (1000 m), respectively.

Vertical and horizontal mixing of momentum and heat/salt are represented by a Laplacian formulation with prescribed eddy viscosities A_H and A_V and eddy diffusivities K_H and K_V, respectively. To look at the effect of varying diffusivities, we will consider both constant values of $\bar{K}_V$ and $\bar{K}_H$ (as were used in Dijkstra and Weijer, 2005) and depth dependent values according to (Bryan and Lewis, 1979; England, 1993)

$$K_V(z) = \kappa_V \left[K_V^0 - A_s \arctan \lambda(z - z_*) \right], \tag{1a}$$

$$K_H(z) = K_H^0 + \left(A_r - K_H^0 \right) e^{\frac{z}{500}}, \tag{1b}$$

with $z \in [-5000, 0]$ m. Here, $K_H^0 = 0.5 \times 10^3$ m^2 s^{-1}, $A_r = 1.0 \times 10^3$ m^2 s^{-1}, $K_V^0 = 8.0 \times 10^{-5}$ m^2 s^{-1}, $A_s = 3.3 \times 10^{-5}$ m^2 s^{-1},
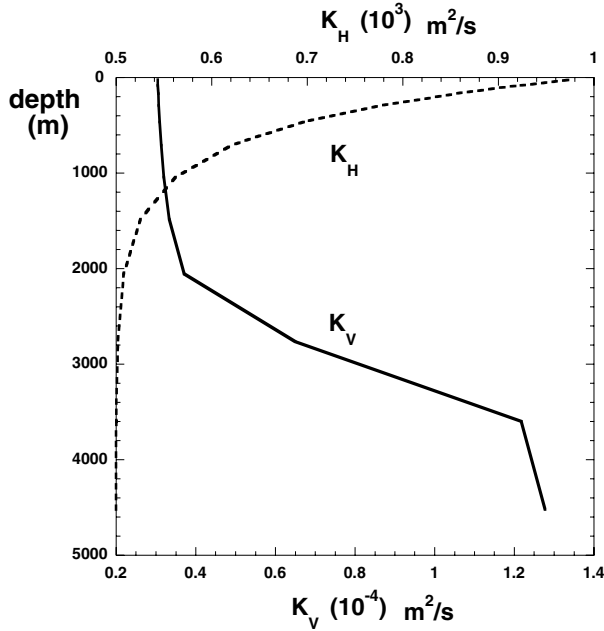
Fig. 1. Spatial distribution of the mixing coefficients $K_V(z)$ (solid, lower x-axis) and $K_H(z)$ (dashed, upper x-axis) in (1) for $\kappa_V = 1.0$.

$\lambda = 4.5 \times 10^{-3}$ m^{-1}, $z_* = -2.5 \times 10^3$ m; κ_V is a parameter which will be specified later on.

The spatial patterns of both $K_V(z)$ and $K_H(z)$ are shown for $\kappa_V = 1$ in Fig. 1. The vertical diffusivity K_V increases from 3.1×10^{-5} m^2 s^{-1} at the surface to 1.3×10^{-4} m^2 s^{-1} near the bottom of the flow domain. The horizontal diffusivity K_H increases monotonically from 5.0×10^2 m^2 s^{-1} at the bottom of the ocean to about 1.0×10^3 m^2 s^{-1} near the surface.

The ocean flow is forced by the annual-mean wind stress as given in Trenberth et al. (1989). The upper ocean is coupled to a simple energy-balance atmospheric model (see appendix in Dijkstra and Weijer, 2005) in which only the heat transport is modelled (no moisture transport). The freshwater flux will be prescribed in each of the results below. The model has no sea-ice component. As in low-resolution ocean GCMs, the surface forcing is represented as a body forcing over the upper layer. On the continental boundaries, no-slip conditions are prescribed and the heat and salt fluxes are zero. At the bottom of the ocean, both the heat and salt fluxes vanish and slip conditions are assumed.

2.2. Methods

We determine steady-state solutions of the model as described in Section 2.1 versus parameters using continuation methods (Dijkstra, 2005). The discretized steady equations can be written as a non-linear algebraic system of equations of the form

$$\mathbf{F}(\mathbf{x}, \lambda) = 0, \tag{2}$$

where $\mathbf{x}$ is the state vector and λ is one of the parameters (or the control parameter). For the global ocean model (with a 4° horizontal resolution and 12 layers in the vertical) the dimension of the state space (and of $\mathbf{x}$) is 284 544.

As in Dijkstra and Weijer (2005), the procedure to compute bifurcation diagrams of the model is:

(i) Under restoring conditions for the surface salinity field (Levitus, 1994), a steady solution is determined for 'most realistic' values of the parameters of the model.

(ii) From this steady solution the freshwater flux, say F_S^e, is diagnosed.

(iii) An anomalous freshwater flux F_S^p over a region near New Foundland with domain $(\phi, \theta) \in [60°\,W, 24°\,W] \times [54°\,N, 66°\,N]$ is prescribed in addition to F_S^e with strength γ_p Sv. With $F_S^p = 1$ in this domain and zero outside, then the total freshwater flux is prescribed as

$$F_S = F_S^e + \gamma_p F_S^p - Q, \tag{3}$$

where the quantity Q is determined such that

$$\int_{S_{oa}} F_S \, r_0^2 \cos\theta \, \mathrm{d}\theta \mathrm{d}\phi = 0, \tag{4}$$

and S_{oa} is the total ocean surface.

(iv) A branch of steady solutions versus γ_p is calculated under the freshwater forcing (3), starting from the solution determined under (i) for $\gamma_p = 0$.

For clarity, we illustrate the connection between the hysteresis behaviour in ocean models (or EMICs) on one hand and bifurcation diagrams on the other hand with help of Fig. 2. In the bifurcation diagram in Dijkstra and Weijer (2005), schematically shown in Fig. 2a, the strength of the AMOC (ψ) of each steady state is plotted versus γ_p; one branch of solutions was found. A solid linestyle along the branch indicates that steady solutions are stable while steady states are unstable on the dashed part of the branch. There are two saddle-node bifurcations, indicated by L_- and L_+, respectively which separate the stable and unstable parts of the branch.

In quasi-equilibrium simulations, γ_p is extremely slowly varied in time and the following is observed (Fig. 2b). Starting at the reference solution for $\gamma_p = 0$, the upper solution branch in Fig. 2a is followed until the value of L_+ where no nearby steady-state solution exists anymore. Hence, the solution changes rapidly ('collapse' in Fig. 2b) to that on the lower branch and follows that branch with increasing γ_p. If from a large value of γ_p, the solution is followed with decreasing γ_p then the lower branch is followed up to the value of γ_p at L_-, where a transition ('recovery' in Fig. 2b) occurs to the solution on the upper branch.

Let the value of γ_p at the $L_\pm$ be indicated by $\gamma_p^\pm$, respectively, then the width of the hysteresis, say Δ_H, is given by
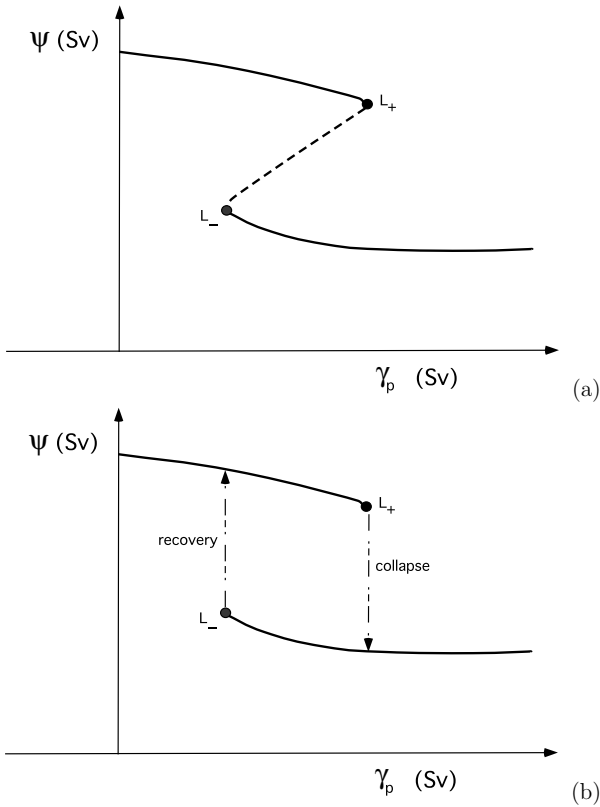
$$\Delta_H = \gamma_p^+ - \gamma_p^-. \tag{5}$$

Fig. 2. (a) Sketch of the bifurcation diagram with two saddle-node bifurcations labeled L_- and L_+. Solid parts of the branch indicate stable steady solutions and steady states are unstable along the dashed part of the branch. (b) Typical hysteresis behaviour when γ_p is increased slowly in time from zero up to large values and back. Near the saddle-node bifurcations in (a) the solution jumps from one stable steady state to another. The direction of these transient jumps are indicated with an arrow.

In typical ocean model studies, where γ_p is varied with about 0.05 Sv/1000 yr, one finds approximations of the value of Δ_H because the jumps are not really 'vertical' as in Fig. 2b. The typical hysteresis diagrams that were computed in Rahmstorf et al. (2005) show that it is not easy to define Δ_H accurately from these simulations. With continuation methods, one is able to determine the hysteresis width very accurately as the values of γ_p at $L_\pm$ are computed explicitly.

3. Results

In the first subsection below (Section 3.1), we consider the sensitivity of the bifurcation diagram of the global ocean model (as presented in Section 2.1) versus horizontal and vertical diffusivities in the model. It will turn out that the saddle-node bifurcations shift with different choices of the diffusivities. In Section 3.2, we study the physics of the saddle-node bifurcations using integral balances of the steady flows. This characterization will be used

in Section 3.3 to study the physics of the shift in the saddle-node bifurcations with changes in the diffusivities.

3.1. Bifurcation diagrams for different diffusivities

If we take $\kappa_V = 1.0$ in eq. (1a), then we find an AMOC strength of about 9 Sv for the reference (unperturbed) solution at $\gamma_p = 0.0$. As this is quite small, we increased κ_V to a value of $\kappa_V = 4.1$ such that the AMOC strength at $\gamma_p = 0.0$ is 14.2 Sv. For this case, the vertical diffusivity K_V increases from $1.2 \times 10^{-4}\,\mathrm{m^2\,s^{-1}}$ at the surface to $5.3 \times 10^{-4}\,\mathrm{m^2\,s^{-1}}$ near the bottom of the flow domain. The horizontal diffusivity is as in eq. (1b). The bifurcation diagram for this case is plotted as the curve **d** in Fig. 3a.
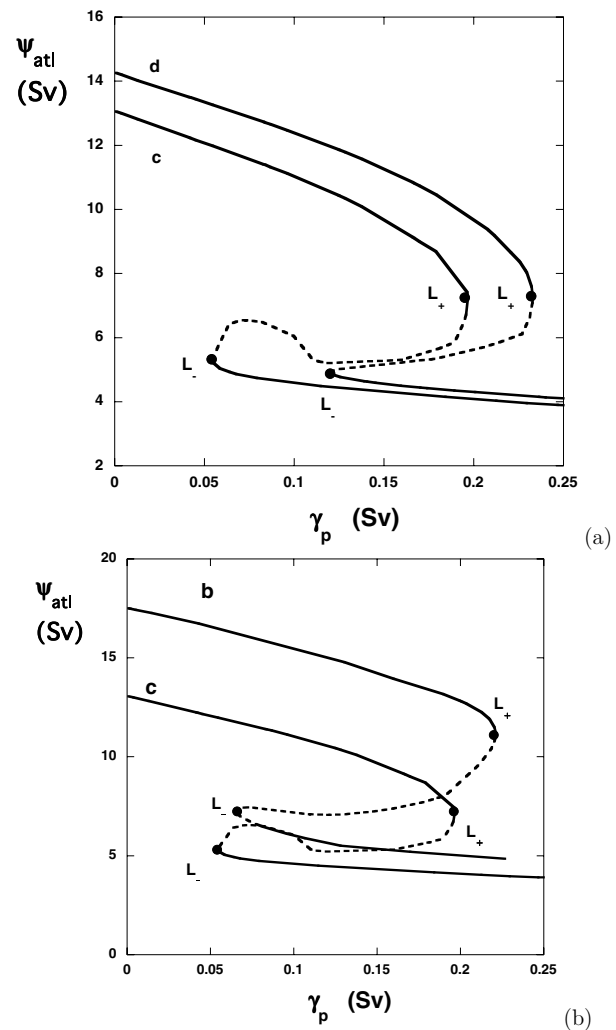

Fig. 3. Bifurcation diagrams where the strength of the AMOC (ψ_{atl}) is plotted versus the strength of the anomalous freshwater forcing (γ_p). (a) Cases **d** and **c**, with **d**: K_V and K_H as in eq. (1) with $\kappa_V = 4.1$; **c**: K_V as in eq. (1a) with $\kappa_V = 4.1$ and constant $\bar{K}_H = 5 \times 10^2\mathrm{m^2s^{-1}}$. (b) Cases **c** and **b**, with **c** as in (a) and **b**: constant $\bar{K}_V = 3.4 \times 10^{-4}\mathrm{m^2s^{-1}}$ and constant $\bar{K}_H = 5 \times 10^2\mathrm{m^2s^{-1}}$.

To study the effect of the shape of the horizontal diffusivity, we also determined the bifurcation diagram for the same distribution of $K_V(z)$, but with a constant $\bar{K}_H = 500 \, \text{m}^2 \, \text{s}^{-1}$; this curve is plotted as **c** in Fig. 3a. Note that for each case, the reference solution is computed under restoring conditions, such that at $\gamma_p = 0$ the freshwater flux is able to maintain the surface Levitus salinity field. Along the curves **c** and **d**, the surface freshwater flux is therefore slightly different.

Clearly, for the case of a vertically increasing K_H (case **d**), the saddle-node bifurcations have shifted to the right with respect to those of constant $\bar{K}_H$ (case **c**). Values of γ_p at L_- and L_+ for case **c** are given by $\gamma_p = 0.054$ Sv and $\gamma_p = 0.195$ Sv, respectively, giving a $\Delta_H = 0.141$ Sv. For case **d**, values of γ_p at L_- and L_+ are given by $\gamma_p = 0.120$ Sv and $\gamma_p = 0.232$ Sv with a $\Delta_H = 0.112$ Sv. An increasing horizontal diffusivity in the upper ocean therefore decreases the hysteresis width.

To determine the effect of the vertical shape of the vertical diffusivity we consider the case **b** with constant $\bar{K}_V = 3.4 \times 10^{-4} \text{m}^2\text{s}^{-1}$ and $\bar{K}_H = 5 \times 10^2 \text{m}^2\text{s}^{-1}$. Motivation for the value of $\bar{K}_V$ is that it is about the vertical mean of the profile used in **d**. Using much larger values of $\bar{K}_V$ leads to significantly different freshwater fluxes in the reference solution at $\gamma_p = 0$ which troubles the comparison between the different cases. The bifurcation diagram for case **b** is plotted in Fig. 3b together with that of case **c**. The reference (unperturbed) solution at $\gamma_p = 0.0$ has a stronger AMOC in case **b** than in case **c**. This is easily explained as there is stronger vertical mixing in the upper ocean which is responsible for a deeper thermocline and hence a stronger overturning. For case **b**, values of γ_p at L_- and L_+ are given by $\gamma_p = 0.066$ Sv and $\gamma_p = 0.22$ Sv with a $\Delta_H =$

0.154 Sv. An increased vertical diffusivity in the upper ocean hence gives a slightly increased hysteresis width and a shift of the saddle-node bifurcations to larger values of γ_p.

Solutions of the AMOC along several points of the curve **d** in Fig. 3a are plotted in Fig. 4. For small γ_p, the solution of the AMOC is near to the unperturbed state with strong northern sinking and no bottom water of southern origin (Fig. 4a). Along the bifurcation diagram, the strength of the AMOC decreases for increasing γ_p until the saddle-node bifurcation at L_+ (Fig. 3a). In the pattern of the AMOC, the return flow shallows (Fig. 4b) and the deep flow from the south strengthens. Once on the unstable branch of steady states from L_+ to L_-, this southern sinking component increases (Fig. 4c) leading eventually to the stable collapsed state (Fig. 4d) for values of γ_p on the lower (drawn) branch in Fig. 3a.

From these bifurcation diagrams, we can qualitatively explain the results in Manabe and Stouffer (1999) in terms of the shift of the saddle-node bifurcations (as in Fig. 3b). In their first simulation with a vertically dependent K_V (as our case **c**), they find a transition to a stable collapsed state and hence for this simulation the system is in the multiple equilibrium regime. This implies that their reference state has a freshwater flux comparable to a value of γ_p (here in our model) which is located between L_- and L_+ for case **c** in Fig. 3b, that is, for $0.054 < \gamma_p < 0.195$ Sv. In their second simulation, they use enhanced but constant vertical diffusivity (as our case **b**) and do not find a collapsed stable equilibrium state. Hence, their freshwater flux in the unperturbed state then corresponds to a value of γ_p in our model located left of L_- for case **b** in Fig. 3b. The only possible situation consistent with both results is when γ_p is located within the interval
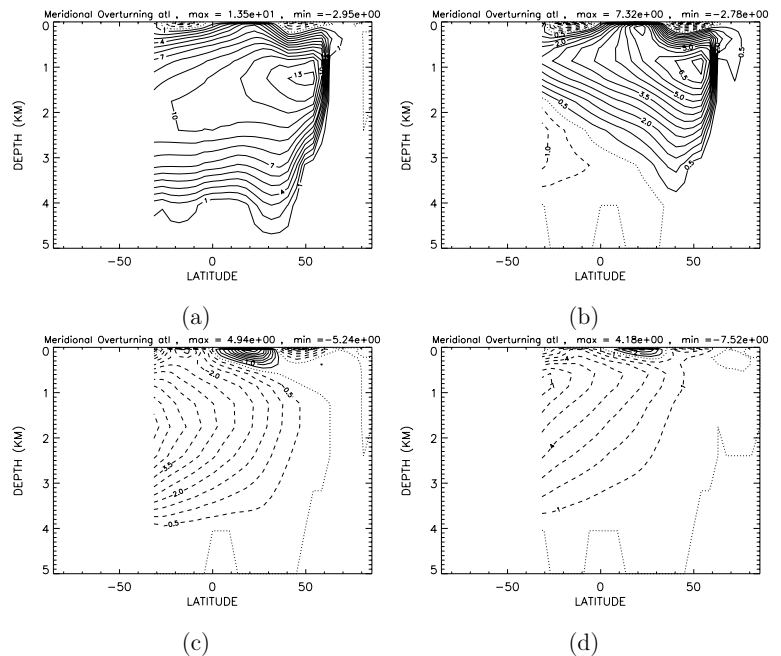

Fig. 4. Contour plot of the AMOC for several values of γ_p along curve **d** in Fig. 3a. Contour values are in Sv: (a) $\gamma_p = 0.042$ Sv, $\psi_{\text{atl}} = 13.5$ Sv; (b) $\gamma_p = 0.23$ Sv, $\psi_{\text{atl}} = 7.3$ Sv; (c) $\gamma_p = 0.12$ Sv, $\psi_{\text{atl}} = 4.9$ Sv and (d) $\gamma_p = 0.23$ Sv, $\psi_{\text{atl}} = 4.2$ Sv.

$0.054 < \gamma_p < 0.066$ Sv, hence between both saddle-node bifurcations L_- in Fig. 3b.

Note that this is only a small interval over the whole domain but the importance here is that with increasing upper ocean vertical mixing, the bifurcation diagram shifts to the right and hence such an interval always exists. The effect is even larger when the horizontal diffusivity is increased (Fig. 3a). As a consequence the range of γ_p of the multiple equilibria regime shifts to larger values and hence becomes less likely (as the freshwater flux becomes more and more unrealistic). This does not yet explain the physics of the results in Manabe and Stouffer (1999). The problem can, however, be formulated much sharper now: what physics characterizes the value of γ_p at L_-?

3.2. Characterization of the saddle-node bifurcation L_-

Using a simple box model, it was already pointed out by Rahmstorf (1996) that the multiple equilibrium regime was related to the net freshwater budget over the Atlantic basin. This issue was revisited by De Vries and Weber (2005) who showed (using an EMIC) that the sign of the net freshwater import by the AMOC near 35°S in the Atlantic is very likely controlling whether a stable collapsed state exists or not.

As the saddle-node bifurcations only exist because of the salt-advection feedback (Dijkstra, 2005), this motivates to consider the integral balance of salt (fresh water) over the Atlantic domain, say V, bounded by the latitudes θ_s and θ_n. When the stationary salinity equation is integrated over V, we obtain

$$\int_{S_{oa}} S_0(P - E) r_0^2 \cos\theta \, \mathrm{d}\phi \, \mathrm{d}\theta = \Phi(\theta_n) - \Phi(\theta_s), \tag{6}$$

where the left-hand side is the freshwater volume (in Sv) going through the ocean–atmosphere surface S_{oa} and the right-hand side is the net freshwater transport (in Sv) through the lateral boundaries at θ_n and θ_s. The freshwater flux Φ is defined as

$$\Phi(\theta) = -\int_{S_\theta} \left(vS - \frac{K_H}{r_0} \frac{\partial S}{\partial \theta} \right) r_0 \cos\theta \, \mathrm{d}\phi \, \mathrm{d}z, \tag{7}$$

where S_θ is the zonal ocean section at latitude θ.

As we computed exact steady states (up to discretization error), the balance (eq. 6) is satisfied accurately. In Fig. 5, the different terms are plotted along the bifurcation diagram of case **d** in Fig. 3a. The integral of $E - P$ (**emp**) is linear in γ_p by construction as fresh water is put into the northern North Atlantic and this flux decreases with γ_p. All terms (diffusive and advective) are of the same order of magnitude and balance up to an accuracy of about 0.1% of the magnitude of the largest individual term. The balances are of the same accuracy for the other cases **b** and **c** in Fig. 3.

If we introduce $\bar{v}, \bar{S}, \langle v \rangle$ and $\langle S \rangle$ through

$$\bar{v} = \int v \cos\theta \, \mathrm{d}\phi; \quad \langle v \rangle = \frac{\bar{v}}{\int \cos\theta \, \mathrm{d}\phi}, \tag{8a}$$
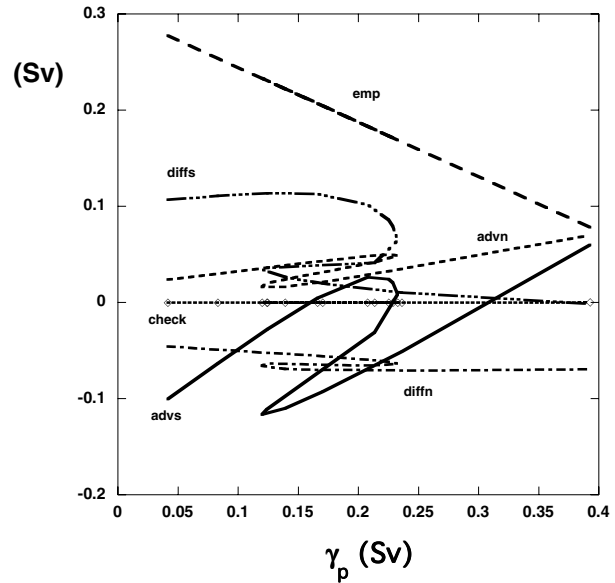

Fig. 5. Terms in the freshwater balance (eq. 6) for case **d** in Fig. 3a, where **advn** is the integral of vS over the section at $\theta = 60$N, **advs** is the integral of vS over the section at $\theta = 35$S, **diffn** is the integral of $(K_H/r_0) \, \partial \, S/\partial \, \theta$ over the section at $\theta = 60$N, **diffs** is the integral of $(K_H/r_0) \, \partial \, S/\partial \, \theta$ over the section at $\theta = 30$S, and **emp** is the surface integral of $S_0(E - P)$. In this case **advn – difn – (advs - difs) – emp = check** is zero up to a relative accuracy of 0.1%. All units are in Sverdrup.

$$\bar{S} = \int S \cos\theta \, \mathrm{d}\phi; \quad \langle S \rangle = \frac{\bar{S}}{\int \cos\theta \, \mathrm{d}\phi}, \tag{8b}$$

then we have the identities

$$\int (v - \langle v \rangle) \cos\theta \, \mathrm{d}\phi = 0; \quad \int (S - \langle S \rangle) \cos\theta \, \mathrm{d}\phi = 0. \tag{9}$$

With $v' = v - \langle v \rangle$ and $S' = S - \langle S \rangle$, we can write

$$\int_{S_\theta} vS \cos\theta \, \mathrm{d}\phi \, \mathrm{d}z = \int_{S_\theta} \langle v \rangle \langle S \rangle \cos\theta \, \mathrm{d}\phi \, \mathrm{d}z$$
$$+ \int_{S_\theta} v'S' \cos\theta \, \mathrm{d}\phi \, \mathrm{d}z. \tag{10}$$

If we integrate the continuity equation over the volume, we get

$$\int_{S_\theta} v \cos\theta \, \mathrm{d}\phi \, \mathrm{d}z = 0 \rightarrow \int \bar{v} \, \mathrm{d}z = \int \langle v \rangle \, \mathrm{d}z = 0. \tag{11}$$

Following De Vries and Weber (2005), we define M_{ov} (the overturning component) and M_{az} (the azonal component) as

$$M_{ov}(\theta) = -\frac{r_0}{S_0} \int_{S_\theta} \bar{v}(\langle S \rangle - S_0) \, \mathrm{d}z; \quad M_{az}(\theta) = -\frac{r_0}{S_0} \int_{S_\theta} \overline{v'S'} \, \mathrm{d}z. \tag{12}$$

The expression (10) can then be written as

$$-\frac{1}{S_0} \int_{S_\theta} vS \, r_0 \cos\theta \, \mathrm{d}\phi \, \mathrm{d}z = M_{ov}(\theta) + M_{az}(\theta). \tag{13}$$

De Vries and Weber (2005) have indicated that the sign of $M_{ov}(\theta_s)$, with $\theta_s = 35S$, may be a good indicator for the presence of the multiple equilibrium regime.

As the positions of the saddle-node bifurcations are accurately known here this hypothesis can be tested. We consider $M_{ov}(\theta_s)$ for case **d** together with a more general indicator

$$\Sigma(\theta_s, \theta_n) = M_{ov}(\theta_s) - M_{ov}(\theta_n). \tag{14}$$

Here θ_s and θ_n indicate the latitudes of the northern and southern section, respectively, where the advective freshwater transport by the meridional overturning circulation is computed.

In Fig. 6a, the indicator $M_{ov}(\theta_s)$ is plotted for four different values of θ_s. The locations of the saddle-node bifurcations ($L_{\pm}$) can be seen from the curve but they are also indicated by the vertical dotted lines. Indeed, for the values of θ_s chosen, $M_{ov}(\theta_s)$ is close to zero and the best value of θ_s would be between 25S and 30S. The indicator $\Sigma(\theta_s, \theta_n)$ is plotted for case **d** in Fig. 6b for $\theta_n = 60N$ and four different values of θ_s. For this case, the indicator Σ with $\theta_s = 35S$ exactly passes through zero at the first saddle-node bifurcation. This at first sight provides an attractive indicator, because 60N is exactly in the sinking region (Fig. 4a) and 35S is at the southern tip of Africa. There is, however, also a slight sensitivity to the northern boundary as can be seen in Fig. 6c. It appears that a southward shift in southern boundary shifts the first zero of the curve to smaller values of γ_p. A northward extension of the northern boundary has the same effect.

In spite of this small sensitivity to the precise latitudes of the section, Σ as well as M_{ov} are adequate indicators of the multiple equilibrium regime. Although $M_{ov}(\theta_n)$ is small compared to $M_{ov}(\theta_s)$, it is not negligible and physically it is the net advective freshwater flux by the AMOC which determines whether multiple states exist or not. In the multiple equilibria regime, the AMOC is exporting freshwater [$\Sigma(\theta_s, \theta_n) < 0$ while still the evaporation exceeds precipitation as **emp** > 0 in Fig. 5]; the excess salt is exported out of the basin by the wind-driven gyres.

It is interesting that the indicator Σ is determined by properties just over the region in the Atlantic where the dynamics associated with the salt-advection feedback is active. Indeed, if $\Sigma < 0$ and the northern North Atlantic sea surface is subjected to a perturbation freshwater flux, then the AMOC weakens. As a consequence, the freshwater export by the AMOC decreases which makes the basin even fresher and hence the original instability is amplified. On the other hand when $\Sigma > 0$, such a freshwater perturbation also weakens the AMOC but now the export of salt is decreased which effectively opposes the original perturbation. Although these arguments are far from a detailed result on conditional stability in the multiple equilibrium regime, they provide an intuitive notion why the sign of Σ is likely to be important.
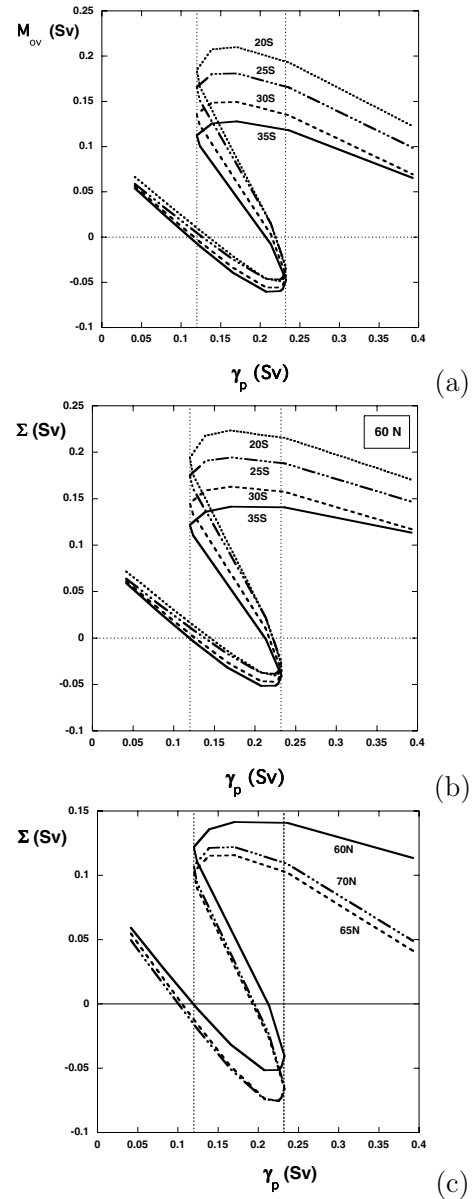

Fig. 6. Indicator functions along the bifurcation diagram of case **d** in Fig. 3a. The vertical lines indicate the positions of L_- and L_+. The part of the branch going from L_+ to L_- represents unstable steady states. (a) $M_{ov}(\theta_s)$ for several values of θ_s. (b) $\Sigma(\theta_s, \theta_n)$ for $\theta_n = 60N$ for several values of θ_s. (c) $\Sigma(\theta_s, \theta_n)$ for $\theta_s = 35S$ for several values of θ_n.

3.3. The physics of the shift in the saddle-node L_-

It was shown in Section 3.1 that a shift in L_- to larger values of γ_p occurred when the vertical diffusivity was changed from the vertical profile in case **c** to the constant value in case **b**. In Section 3.2, it was shown that a sign change in Σ provides a good indicator for the position of the saddle-node bifurcation L_-. To determine the physics of the shift in L_-, we have to investigate the changes in the freshwater budget contributions to
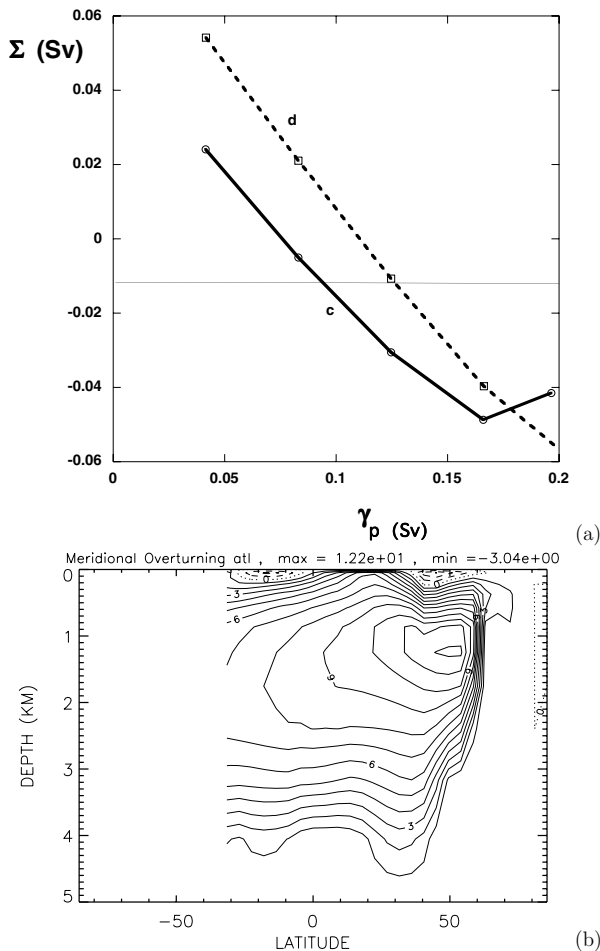
Fig. 7. (a) Comparison of $\Sigma(\theta_s, \theta_n)$ with $\theta_s = 35S$ and $\theta_n = 60N$ along the upper branch of the bifurcation diagram in Fig. 3a for both cases **c** and **d**. (b) Contour plot of the Atlantic meridional overturning streamfunction for $\gamma_p = 0.042$ Sv ($\psi_{atl} = 12.2$ Sv) for case **c**.

Σ due to the changes in the vertical diffusivity. The same holds for the changes in horizontal diffusivity where also L_- shifts to large values of γ_p from the constant value used in case **c** to the vertical profile in case **d**. Since the change in L_- is much larger between the cases **c** and **d** (Fig. 3a), we analyse these in more detail.

We choose $\theta_s = 35S$, $\theta_n = 60N$ and show Σ for both cases **c** and **d** (Fig. 7a) along the upper branch of the bifurcation diagram in Fig. 3a. The value of Σ for case **c** is still slightly positive in L_- (actually Σ is approximately zero at L_- for $\theta_n = 70N$) but it is still a good indicator of the multiple equilibrium regime. The curve for case **c** is below that of case **d** which is in agreement with the shift in L_- to the right in going from **c** to **d**. The meridional overturning streamfunction for case **c** is for $\gamma_p = 0.042$ Sv (Fig. 7b) only slightly weaker than that of case **d** (Fig. 4a) but the pattern is similar.

To diagnose the cause of the change in Σ in case **d**, the zonal mean values of the meridional velocity $\langle v \rangle$ and salinity $\langle S \rangle$ are

shown in Fig. 8 for four values of γ_p. Both salinity (Fig. 8a) and velocity profiles (Fig. 8c) hardly change with γ_p at the northern boundary 60N. At 35S, however, the solutions become less saline at the bottom and more saline at the top (Fig. 8b) due to the decrease in meridional overturning (Fig. 8d). This indicates that the sign of Σ is linked to the strength of the overturning. When the overturning is decreased, less salt is transported out of the basin, and hence Σ decreases and eventually becomes negative.

The cause of the different Σ values between the cases **c** and **d** is shown for $\gamma_p = 0.042$ Sv in Fig. 9. For the same value of γ_p, the overturning is larger is case **d** (Fig. 9b) due to the larger horizontal diffusivity (and in this z-coordinate model also a slightly larger vertical diffusivity due to the Veronis effect). The zonal mean meridional velocity $\langle v \rangle$ is more negative in deeper layers in case **d** while the salinity is larger (Fig. 9a). This causes a larger outflow of salt in case **d** and hence a larger positive value of Σ (Fig. 9c). The same holds for the differences between the cases **b** and **c**, as due to the upper ocean increase in K_V also the AMOC increases, but the differences in Σ are smaller than those between the cases **c** and **d**.

4. Summary and discussion

Using a fully implicit global ocean model, we revisited the problem of the characterization of the multiple equilibrium (ME) regime of the AMOC. Our main motivation was to explain the climate model results on the apparent sensitivity of the ME regime to the vertical dependence and amplitude of the horizontal and vertical diffusivities (Manabe and Stouffer, 1999). Although our ocean model certainly has deficiencies (Dijkstra and Weijer, 2005), the main advantages are that (i) full bifurcation diagrams can be computed versus the freshwater input γ_p and (ii) the sensitivity of these diagrams to changes in the diffusivities can be efficiently calculated.

First main point is that changes in K_V and K_H lead only to quantitative changes in the position of the saddle-node bifurcations. There is no qualitative change in the bifurcation diagram in that the ME regime disappears. Hence, although the results in Manabe and Stouffer (1999) suggest an enormous sensitivity to the shape and amplitude of K_V, this sensitivity is actually quite modest. The bifurcation diagram moves slightly to the right (larger values of γ_p) which indicates that one needs a larger anomalous freshwater flux in the northern North Atlantic to maintain both stable overturning states. Of course, qualitative changes may occur when larger changes in shape and amplitude of K_V are considered.

To understand the physics of this shift in the bifurcation diagram, we followed up on earlier ideas (Rahmstorf, 1996; De Vries and Weber, 2005) to find a scalar indicator Σ whose sign determines whether a solution is in the ME regime or not. Because we can compute the position of the saddle-node bifurcations accurately, we slightly improve on the indicator suggested by De Vries and Weber (2005) and show that it is better
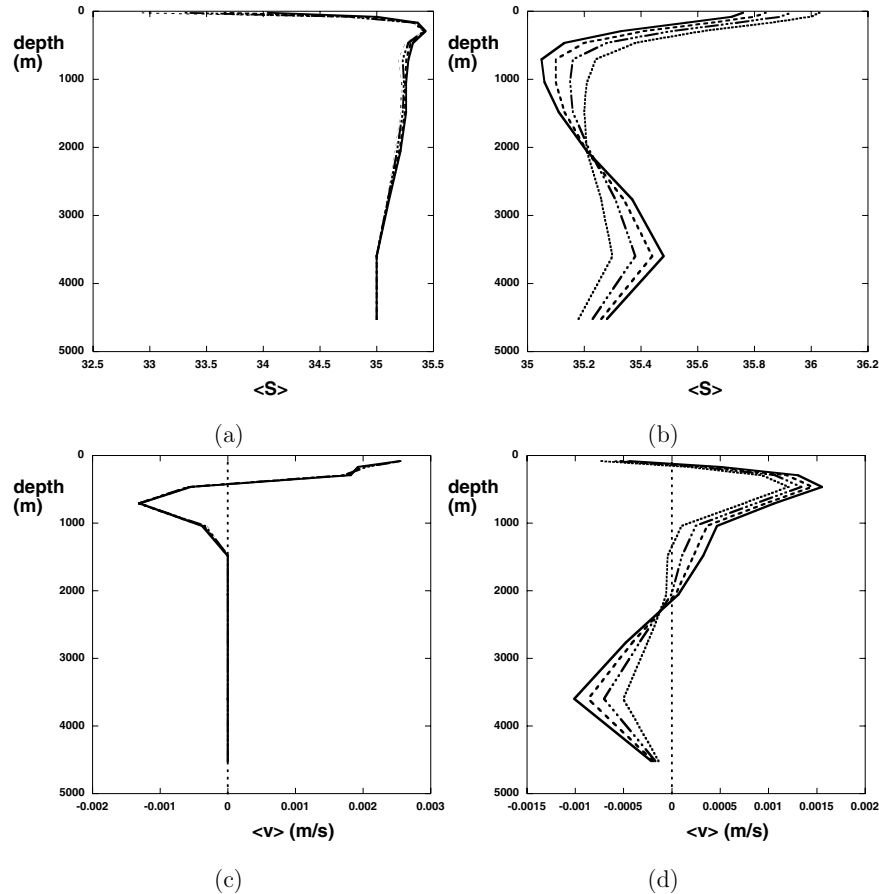
Fig. 8. Profiles of the zonal mean salinity and the meridional velocity along the upper branch of the bifurcation diagram Fig. 3a for case **d**. (a) $\langle S \rangle$ at $\theta_n = 60N$, (b) $\langle S \rangle$ at $\theta_s = 35S$, (c) $\langle v \rangle$ at $\theta_n = 60N$, (d) $\langle v \rangle$ at $\theta_s = 35S$. The linestyle indicates successive values of γ_p with (solid) $\gamma_p = 0.042$ Sv, (dashed) $\gamma_p = 0.083$ Sv, (dash-dotted) $\gamma_p = 0.125$ Sv and (dotted) $\gamma_p = 0.166$ Sv.

to include the freshwater transport by the AMOC at the northern boundary into Σ. It was shown that if $\Sigma < 0$, that is, net freshwater output by the AMOC, then the global ocean flow is in the ME regime.

A plausible physical argument why Σ may be a good indicator was given in Section 3.2. There likely is a more fundamental reason why the boundaries at 35°S and 60°N are the appropriate latitudes in this indicator. It is, however, not easy to address this conditional stability problem as it is highly non-linear. One has to demonstrate that, under conditions of $\Sigma < 0$ there exists a finite amplitude perturbation which, when applied to one stable state, gives a transition to the other stable state (Straughan, 2004). This difficult issue is left for further study.

It is interesting that Σ is influenced by both northern input (Bering Strait) and southern input (Agulhas, Drake Passage) of fresh water. If the global ocean state is close to that with $\Sigma = 0$, small changes in the salinity of the inflow of this water may be responsible for a transition to the ME regime. For example, additional salt input from the Agulhas Leakage will increase the salt content of the Atlantic basin. Hence, the AMOC is expected to become stronger but it depends on the profile of the lateral

inflow (Weijer et al., 1999, 2001) whether this will lead to a decrease or increase in Σ.

To study the physics of the shift of the saddle-node bifurcation L_- we analysed the contributions of the zonal mean profiles of S and v to the value of Σ. It turns out that upper ocean increases in diffusivity lead to changes in the AMOC leading to a larger salinity export and therefore to more positive values in Σ (more salt export by the AMOC). Hence, the saddle-node bifurcation L_- shifts to larger values of γ_p.

In many of the currently state-of-the-art coupled GCMs, it turns out to be difficult to find a collapsed state of the AMOC. This has lead some to the view that the ME regime is no longer present in these GCMs. From the results of this study we can conclude that there are basically two possibilities explaining these GCM results.

(i) The ME regime has indeed disappeared. This would require a qualitative change in the bifurcation diagram in which the saddle-node bifurcations have disappeared. In this case, there has to be a physical mechanism which counteracts the salt-advection feedback and such a mechanism yet has to be identified.
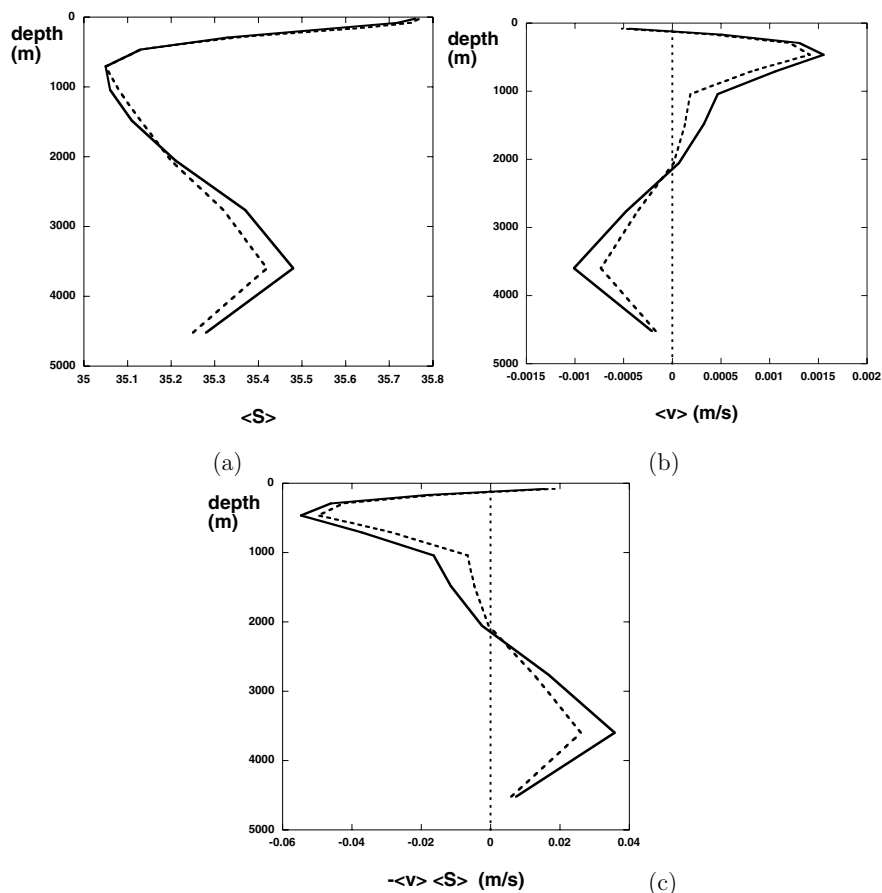
Fig. 9. Vertical profile at $\theta_s = 35S$ of (a) $\langle S \rangle$, (b) $\langle v \rangle$ and (c) $- \langle v \rangle \langle S \rangle$ for both cases **c** (dashed) and **d** (solid) for $\gamma_p = 0.042$ Sv.

Apparently such a mechanism is not present in the Manabe and Stouffer (1999) (older) coupled GCM.

(ii) The ME regime is still present but ocean–atmosphere interaction has moved the bifurcation diagram to the right (outside the realistic freshwater flux regime). In this case, values of Σ must have increased due to the interaction with the atmosphere. There are several processes, for example the dependence of evaporation on temperature and the atmospheric heat transport, which may induce this change in Σ (Weber et al., 2007).

It is at the moment difficult to determine values of Σ from observations. In Weijer et al. (1999), a rough estimate of $M_{\mathrm{ov}}(\theta_s) = -0.2$ Sv ($\theta_s = 30S$) is given which provides an indication that the AMOC is indeed in the ME regime. It would be a very worthwhile attempt to base a value of Σ not only on available hydrographic data but also on satellite data such that the effect of high-frequency variability is taken into account. Maybe the results in this paper will further motivate such an attempt.

5. Acknowledgments

References

Bryan, F. O. 1986. High-latitude salinity effects and interhemispheric thermohaline circulations. *Nature* **323**, 301–304.

Bryan, K. and Lewis, L. J. 1979. A water mass model of the world ocean. *J. Geophys. Res.* **84**, 2503–2517.

Bryden, H. L., Longworth, H. R. and Cunnigham, S. A. 2005. Slowing down of the Atlantic meridional overturning circulation at 25°. *Nature* **438**, 655–657.

Clark, P. U., Pisias, N. G., Stocker, T. F. and Weaver, A. J. 2002. The role of the thermohaline circulation in abrupt climate change. *Nature* **415**, 863–869.

De Vries, P. and Weber, S. L. 2005. The Atlantic freshwater budget as a diagnostic for the existence of a stable shut down of the meridional overturning circulation. *Geophys. Res. Lett.* **32**(No.9), L09606.

Dijkstra, H. A. 2005. *Nonlinear Physical Oceanography: A Dynamical Systems Approach to the Large Scale Ocean Circulation and El Niño, 2nd Revised and Enlarged edition.* Springer, New York, 532 pp.

Dijkstra, H. A. and Weijer, W. 2005. Stability of the global ocean circulation: basic bifurcation diagrams. *J. Phys. Oceanogr.* **35**, 933–948.

England, M. H. 1993. Representing the global-scale water masses in ocean general circulations models. *J. Phys. Oceanogr.* **23**, 1523–1552.

Latif, M., Roeckner, E., Mikolajewicz, U. and Voss, R. 2000. Tropical stabilization of the thermohaline circulation in a greenhouse warming simulation. *J. Climate* **13**, 1809–1813.

Levitus, S. 1994. World Ocean Atlas 1994, Volume 4: Temperature. *NOAA/NESDIS E, US Department of Commerce, Washington DC*, **OC21**, 1–117.

Manabe, S. and Stouffer, R. J. 1994. Multiple-century response of a coupled ocean-atmosphere model to an increase of atmospheric carbon dioxide. *J. Climate* **7**, 5–23.

Manabe, S. and Stouffer, R. J. 1999. Are two modes of thermohaline circulation stable? *Tellus* **51A**, 400–411.

McAvaney, B. 2001. Model evaluation. In: *Climate Change 2001: The Scientific Basis*, Chapter 8 (eds J. T. Houghton, Y. Ding, D. J. Griggs, M. Noguer, P. J. van der Linden and co-editors). Cambridge University Press, Cambridge, UK, pages 225–256.

Rahmstorf, S. 1995. Bifurcations of the Atlantic thermohaline circulation in response to changes in the hydrological cycle. *Nature* **378**, 145–149.

Rahmstorf, S. 1996. On the freshwater forcing and transport of the Atlantic thermohaline circulation. *Clim. Dyn.* **12**, 799–811.

Rahmstorf, S. 2000. The thermohaline circulation: a system with dangerous thresholds? *Clim. Change* **46**, 247–256.

Rahmstorf, S., Crucifix, M., Ganopolski, A., Goosse, H., Kamenkovich, I. and co-authors. 2005. Thermohaline circulation hysteresis: a model intercomparison. *Geophys. Res. Lett.* **L23605**, doi:10.1029/2005GLO23655, 1–5.

Schmittner, A., Latif, M. and Schneider, B. 2005. Model projections of the North Atlantic thermohaline circulation for the 21st century assessed by observations. *Geophys. Res. Lett.* **L23710**, doi:10.1029/2005GLO24368, 1–4.

Stocker, T. F., Wright, D. G. and Mysak, L. A. 1992. A zonally averaged, coupled ocean-atmosphere model for paleoclimate studies. *J. Climate* **5**, 773–797.

Stommel, H. 1961. Thermohaline convection with two stable regimes of flow. *Tellus* **2**, 244–230.

Stouffer, R. J., Yin, J., Gregory, J. M., Dixon, K. W., Spelman, M. J. and co-authors. 2006. Investigating the causes of the response of the thermohaline circulation to past and future climate changes. *J. Climate* **19**, 1365–1387.

Straughan, B. 2004. *The Energy Method, Stability and Nonlinear Convection* 2nd Edition. Springer-Verlag, New York.

Thorpe, R. B., Gregory, J. M., Johns, T. C., Wood, R. A. and Mitchell, J. F. B. 2001. Mechanisms determining the Atlantic thermohaline circulation response to greenhouse gas forcing in a non-flux-adjusted coupled climate model. *J. Climate* **14**, 3102–3116.

Trenberth, K. E., Olson, J. G. and Large, W. G. 1989. *A global ocean wind stress climatology based on ECMWF analyses*. Technical report, National Center for Atmospheric Research, Boulder, CO, USA.

Vellinga, M., Wood, R. A. and Gregory, J. M. 2002. Processes governing the recovery of a perturbed thermohaline circulation in HadCM3. *J. Climate* **15**, 764–780.

Weber, S. L., Drijfhout, S. S., Abe-Ouchi, A., Crucifix, M., Eby, M. and co-authors. 2007. The modern and glacial overturning circulation in the Atlantic ocean in PMIP coupled model simulations. *Climate of the Past* **3**, 51–64.

Weijer, W., De Ruijter, W. P. M., Dijkstra, H. A. and Van Leeuwen, P. J. 1999. Impact of interbasin exchange on the Atlantic overturning circulation. *J. Phys. Oceanogr.* **29**, 2266–2284.

Weijer, W., De Ruijter, W. and Dijkstra, H. A. 2001. Stability of the Atlantic overturning circulation: Competition between Bering Strait freshwater flux and Agulhas heat and salt sources. *J. Phys. Oceanogr.* **31**, 2385–2402.

Weijer, W., Dijkstra, H. A., Oksuzoglu, H., Wubs, F. W. and De Niet, A. C. 2003. A fully-implicit model of the global ocean circulation. *J. Comp. Phys.* **192**, 452–470.

Wood, R. A., Keen, A. B., Mitchell, J. F. B. and Gregory, J. M. 1999. Changing spatial structure of the thermohaline ciirculation in response to atmospheric CO_2 forcing in a climate model. *Nature* **399**, 572–575.